

# Improving solar grade silicon by controlling extended defect generation and foreign atom defect interactions

H.J. Möller · T. Kaden · S. Scholz · S. Würzner

Received: 3 July 2008 / Accepted: 4 November 2008 / Published online: 26 March 2009  
© Springer-Verlag 2009

**Abstract** Multicrystalline silicon has a high commercial potential for solar cell applications. Extended lattice defects, such as dislocations and grain boundaries, are important as recombination and storage centers for metallic impurities. Their control is essential to obtain high efficiencies of the solar cell. Important parameters for the assessment of the final efficiency of the solar cells are the distribution and structure of the defects and their impact on the lifetime of minority carriers. The current understanding of the nucleation mechanisms of the most important defects during crystal growth will be described. Interaction processes between mobile impurities and extended defects are important for the recombination activity. Measurements of the recombination behavior and the contamination level will be presented. Finally, the ramifications on the solar cell efficiency shall be discussed.

**PACS** 61.72.-y · 61.72.Ff · 71.55.Cn

## 1 Introduction

Currently, more than 60% of all commercial solar cells are made from multicrystalline (mc-) silicon. The solar conversion efficiencies are typically in the range of 14 to 16% [1–4], but about 20% have been demonstrated for laboratory cells [5]. The further development is currently driven by cost reduction and efficiency increase. Since about two

thirds of the module cost are silicon material costs, the development of inexpensive silicon feedstock and the efficient use of the material are goals which are currently pursued [6]. A cheaper production process is the direct purification of metallurgical silicon [7], which yields, in general, a feedstock silicon of lower purity. It has been shown that multicrystalline solar cells with 15% efficiency can be made from such a material. This is a cost advantage over monocrystalline silicon, which requires high purity feedstock [8].

More than 80% of multicrystalline silicon is grown by the Bridgman or related techniques. The inevitable slicing steps, however, waste about 50% of the material. Technologies that reduce the number of slicing steps are continuous ribbon growth techniques. Commercially developed are the EFG and the String Ribbon processes, where tubes or sheets are grown [9]. Both production routes yield multicrystalline silicon crystals with different microstructures and impurity levels. This is due to different growth velocity and temperature gradient regimes and the use of different crucible materials.

The performance of multicrystalline solar cells is generally limited by lattice defects, which reduce the minority carrier lifetime. Dislocations, grain boundaries and intragrain defects, such as certain impurities, small clusters of atoms or precipitates, are mainly responsible for the recombination processes. Particularly localized regions of high dislocation densities are known to be rather detrimental [10]. Dislocations and grain boundaries are also important because of their gettering and storage capacity for certain mobile, mainly metallic impurities. If dissolved in the lattice, most of the metal impurities are very recombination active. Because of the high mobility down to lower temperatures they can accumulate at the core of extended defects, which is en-

---

H.J. Möller (✉) · T. Kaden · S. Scholz · S. Würzner  
Institute for Experimental Physics, Technische Universität  
Bergakademie Freiberg, Leipziger Str. 23, 09599 Freiberg,  
Germany  
e-mail: [moeller@physik.tu-freiberg.de](mailto:moeller@physik.tu-freiberg.de)  
Fax: +49-3731-394314

ergetically more favorable. In the bound state, the impurities are, in general, less recombination active.

The total concentration of many impurities that have been analyzed so far exceeds the concentration of the dissolved species by several orders of magnitude. Therefore, in the as-grown material, most of the impurities are bound, mainly at extended defects. These agglomerates of atoms form a reservoir that can release atoms again into the bulk during any thermal steps of the solar cell process. The distribution and concentration in the bulk will depend on the particular thermal process and the binding strength between foreign atom and lattice defect. In most solar cell processes, gettering techniques are applied to remove impurities from the photo-active region. This requires that impurities are less tightly bound and released more easily into the bulk at the gettering temperatures. On the other hand, if they could be tightly bound in the inactive state, one could reduce the recombination centers in the active volume and also increase the efficiency of solar cells.

In order to control the processes better, one needs to know more about the state of the foreign atoms and the interaction processes. The problem became more urgent in recent years because silicon feedstock from different production processes and lower purity is used. In particular, directly purified metallurgical silicon, which contains much higher impurity concentrations, may be increasingly used for cost reasons. These higher impurity contents have to be kept in an inactive state or removed in order to improve the material quality. In the following, the main factors that determine and limit the efficiency will be described, and potential routes for further development shall be discussed.

## 2 Crystal growth of multicrystalline silicon

### 2.1 Ingot techniques

Multicrystalline silicon is either grown by ingot or ribbon techniques [11, 12]. The principles are depicted in Fig. 1(a, b). For the ingot techniques, the crystallization crucibles are either filled with high purity silicon, which is molten inside, or the silicon is molten in a separate crucible and then poured into the crystallization crucible (casting technique). The ingots are crystallized either by the Bridgman or gradient-freeze technique (VGF) and have cross-sections today of more than  $60 \times 60 \text{ cm}^2$  with a weight over 300–400 kg. The crystallization and cooling processes take about 30 to 40 hours, faster production times will be achieved in the future. The heat extraction must occur in a very controlled manner to maintain a high quality of the crystal. In order to achieve a low dislocation density, the melt interface must be kept planar to ensure low thermal stresses.

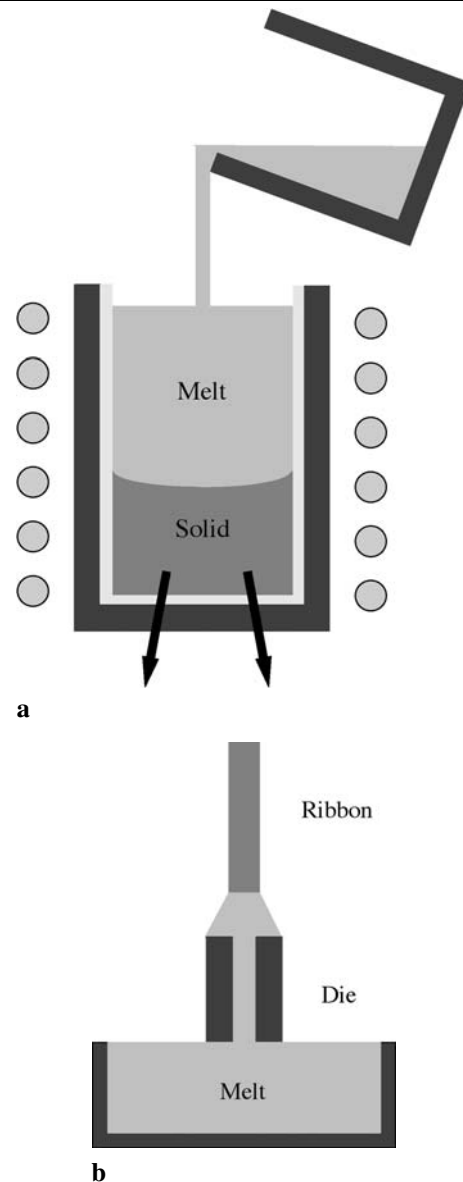


**Fig. 1** Schematic description of ingot and sheet growth processes. **(a)** Ingot casting / Bridgman technique. *Arrows indicate main heat flow.* **(b)** EFG technique (edge-defined-film-fed-growth)

Impurities are present in the silicon feedstock in different concentrations depending on the purification process that has been applied. Particularly the direct purification of metallurgical silicon through solid and melt processes yields less pure feedstock silicon. In addition, impurities are incorporated through the contact of melt and crystal with the crucible walls and the ambient gas atmosphere. Typical crucible materials are  $\text{SiO}_2$  (quartz),  $\text{Si}_3\text{N}_4$  as a coating layer on the inside and graphite from the support die. Dissolution of these materials introduces oxygen, nitrogen and carbon in various concentrations. In addition, remnant impurities in the crucible materials, such as the metals Fe, Cr, Ni or Cu, diffuse into melt and solid. The distribution of impurities

and doping elements along the growth direction by segregation and the formation of precipitates depend on the growth process and the following processing steps. There is also interaction between the various defects, which is complex and certainly not completely understood.

## 2.2 Ribbon techniques

The ribbon or sheet growth techniques require a shaping system to determine the final shape. They differ mainly by the shaping system that is used and can be divided into two categories depending on whether the crystallization direction is parallel or perpendicular to the pulling direction. The RGS method (ribbon-growth-on-substrate) belongs to the latter category [13]. It has the potential of very high production speeds but is still in the development stage. The most advanced method is the edge-defined-film-fed-growth (EFG) technique (Fig. 1(b)). In the industrial process, an octagon tube instead of a sheet is pulled from the melt [14]. The side faces have a width equal to the wafer size and a wall thickness between 200–300  $\mu\text{m}$ . The length of the tube is about 7 m and is mainly determined by the height of the production building. The tubes are cut into the final wafer size by high-powered lasers. A similar technique is the String Ribbon technique where several sheets are grown in parallel [15]. The shaping system consists of two thin heat-resistant filaments at the edges of each ribbon.

The growth velocity of the EFG technique is equal to the crystallization velocity of about 1 cm/min. In order to achieve high production speeds, very high temperature gradients of more than 200 K/cm have to be used at the melt interface. This leads to large thermal stresses in the sheets or tubes and a microstructure consisting of long grain boundaries in growth direction and a high density of dislocations. Another typical feature is the direct contact with the shaping system made from graphite, which introduces a high concentration of carbon into the material. In addition, metal impurities are incorporated from the crucible contact as well.

## 3 Precipitate formation from the melt

The impurities that have to be considered in melt processes are oxygen, carbon and nitrogen. Apart from the introduction through the feedstock silicon, the main contributions come from the direct contact of the melt with the crucible walls, the melt feeding parts and the ambient gas phase. For the ingot techniques (Bridgman, VGF) the melt is in contact with the porous ( $\text{Si}_3\text{N}_4$ ) coating and through the pores with the quartz ( $\text{SiO}_2$ ) crucible. The dissolved amount of oxygen and nitrogen depends on the dissolution rate of  $\text{SiO}_2$

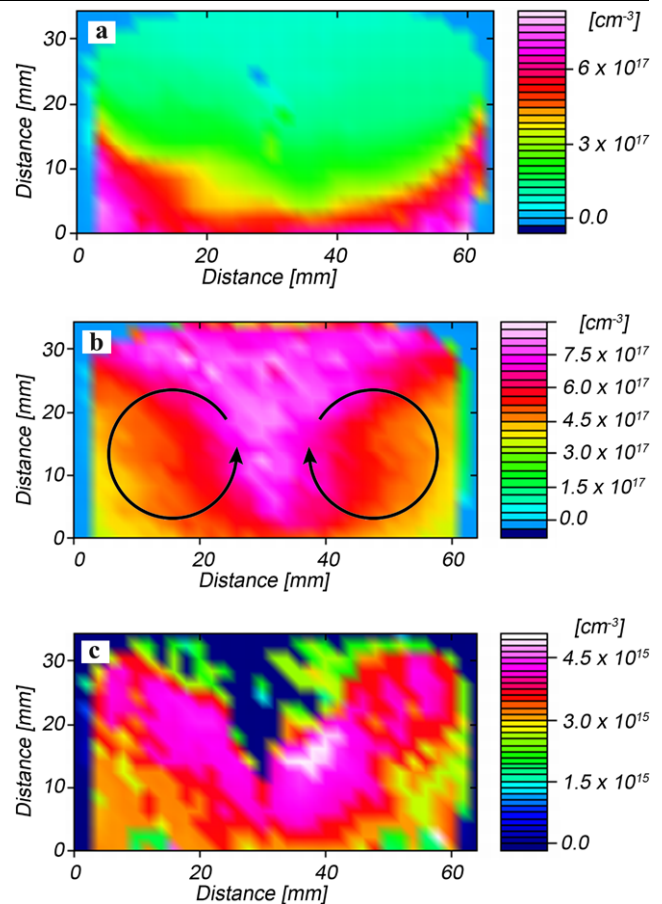


**Fig. 2** Topographic Fourier-transform infrared (FTIR) measurements of the distribution of dissolved oxygen (a), carbon (b) and nitrogen (c) in a vertical cross-section of a multicrystalline silicon crystal grown by the Bridgman technique. The corresponding convection flow in the melt is indicated in (b)

and  $\text{Si}_3\text{N}_4$ . The structural properties of the coating layer (thickness, porosity, etc.) are important here. Furthermore, one has to consider the exchange of gases over the melt surface. Oxygen is lost by evaporation of  $\text{SiO}$ , and carbon is introduced by CO gas that forms through the oxidation of graphite parts in the crystallization furnace. By controlling the flow of ambient gas (e.g., argon) over the melt surface one can influence the amount of oxygen and carbon in the melt.

The impurities are distributed in the melt by convection and diffusion processes. Because of the different segregation coefficients ( $k_0 = 1.4$  for oxygen,  $k_0 = 0.07$  for carbon, and  $k_0 = 0.0007$  for nitrogen) the impurity distributions that are incorporated in the solid differ considerably. Figure 2 shows experimentally determined distributions of dissolved oxygen, carbon and nitrogen in a crystal grown by the Bridgman technique. Carbon and nitrogen are enriched in the center of the crystal, whereas the oxygen distribution follows approximately the shape of the melt interface. The patterns can be

**Fig. 3** Two dimensional simulation with the finite-element method (FEM) of the oxygen distribution (a) in a vertical cross-section of mc-silicon grown in an industrial Bridgman furnace and comparison with experimental FTIR results (b)

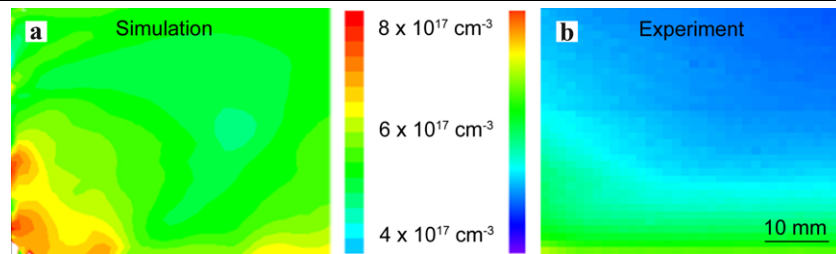
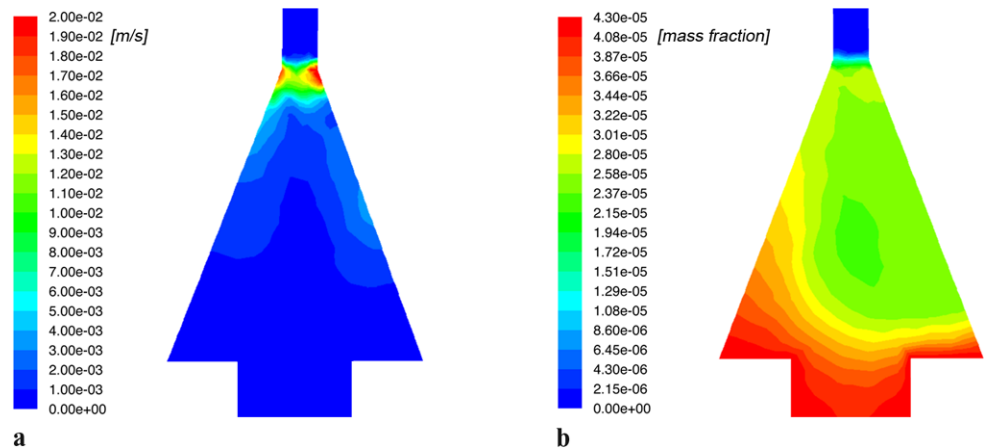


**Fig. 4** Two dimensional FEM simulation of the melt velocity (a) and the distribution of carbon (b) in the meniscus region for the EFG ribbon growth process



explained on the basis of the mass distributions in the melt, which can be simulated today quite accurately by simulation programs. A simulation by the finite-element method (FEM) of a cross-section of the crucible for this particular growth process shows two opposite convection rolls with a flow of melt parallel to the melt surface and an upwards stream in the center (Fig. 2(b)). Since carbon and nitrogen are less incorporated in the solid, the center of the melt will be enriched with these impurities as observed. Depending on the growth conditions, such as growth velocity and gas flow over the melt surface, the enrichment in the melt varies and can even exceed the solubility limit in the melt.

The flow pattern of melts in industrial growth furnaces differs from the depicted situation because of other crucible geometries and a larger melt volume. Figure 3 shows an experimentally determined oxygen distribution in comparison with simulation results [16]. Typical are the decrease of the oxygen concentration in growth direction and the enrichment at the corner of the crucible. The impurity distribution pattern also differs for continuous growth processes. In the EFG ribbon growth, the melt is continuously replenished with fresh, pure silicon feedstock. Therefore, the average impurity concentrations in the melt are determined by the mixing of high purity silicon with the previously enriched melt. The main impurity in EFG ribbons is carbon due to the contact of the melt with the graphite parts of the crucible and the shaping system. Most of the carbon is introduced in the crucible part, which is kept at the highest temperature in the system. The melt feeding system supplies the impu-

rity enriched melt to the meniscus region. The distribution of carbon at the solidification front is again determined by diffusion and convection. Two-dimensional FEM simulations of the carbon distribution show rather high concentrations of about  $6 \times 10^{18} \text{ cm}^{-3}$  (mass fraction  $5 \times 10^{-5}$ ), which is above the solubility limit in the melt of  $5 \times 10^{18} \text{ cm}^{-3}$  at the melting point (Fig. 4).

These and other numerical and experimental investigations of recent years have shown that the concentrations for carbon and nitrogen in the melt may exceed the solubility limit near the melting point both for ingot and ribbon silicon. This can lead to precipitation in the melt. Because of the much higher diffusion coefficient in the melt compared to the solid, large precipitates can grow. In fact, large precipitates of  $\text{Si}_3\text{N}_4$  and  $\text{SiC}$  have been observed in directionally solidified multicrystalline silicon [17–23]. They mainly occur in form of long filaments, needles or tubes that run approximately in growth direction over several mm (Fig. 5).

In EFG ribbons, the growth of large  $\text{SiC}$  layers has been observed [24]. The microstructure of EFG ribbons contains regions of a high density of (111) twin boundaries. Measurements of intrinsic stresses by infrared double diffraction have shown (Fig. 6) that some of these boundaries are highly stressed. This could be explained by the incorporation of monatomic layers of  $\text{SiC}$  precipitates [25, 26]. Because of a shorter  $\text{Si-C}$  bond across the boundary the lattice is contracted here, which causes high local stresses. These layers can extend over several millimeters. It has been suggested that these precipitates (filaments or layers) form directly at



**Fig. 5** Filaments and precipitates of  $\text{Si}_3\text{N}_4$  and  $\text{SiC}$  in a mc-silicon crystal

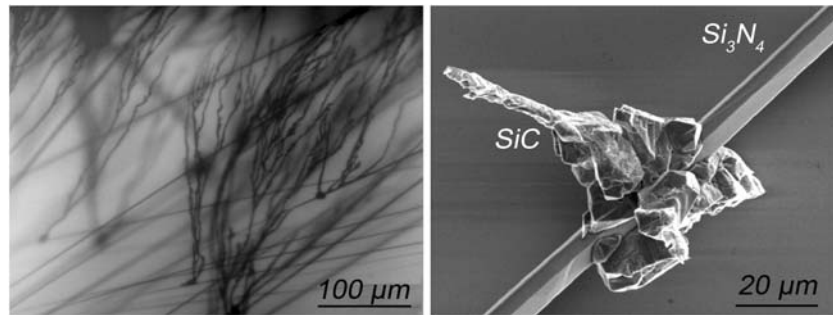
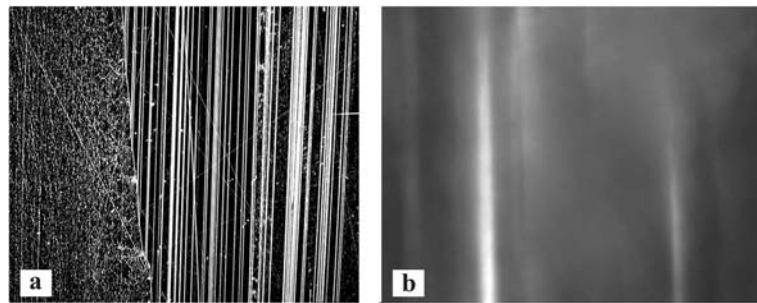


**Fig. 6** Structurally etched surface of an EFG wafer showing lamellae of twin boundaries and dislocations in EFG silicon (a). Infrared double diffraction image showing internal stresses at  $\text{SiC}$  decorated twin boundaries stresses (b)



the melt interface by the following mechanism [11, 27, 28]. Considering carbon and nitrogen, the solidification behavior can be described schematically for low impurity concentrations by a eutectic two component (A, B) phase diagram with an intermediate phase, here of  $\text{Si}_3\text{N}_4$  or  $\text{SiC}$  (Fig. 7). In both cases, there exists a limited solubility in the melt. If the eutectic concentration  $c_e$  at the melt interface is exceeded ( $c_e = 4.6 \times 10^{18} \text{ cm}^{-3}$  for carbon and  $6.4 \times 10^{18} \text{ cm}^{-3}$  for nitrogen), precipitation may occur. Whether the precipitates nucleate in the melt or at the melt–solid interface depends on the supercooling and the availability of nucleation sites. The most probable process is the heterogeneous nucleation at the melt interface because of the lower interface energy with the solid phase. Nucleation may occur at inhomogeneities, such as grain boundaries or dislocations that form at the interface during solidification.

If solidification takes place at a concentration  $c_0$  (of B atoms) above the eutectic concentration  $c_e$  the formation of the second phase would occur at a temperature  $T_1$  in thermodynamical equilibrium. The formation of the second phase, however, requires nucleation and an undercooling of the melt. The most likely process is heterogeneous nucleation at the melt interface because it requires less undercooling. Therefore, the interface temperature has to be lowered first to the temperature  $T_0$  where the liquid begins to solidify and nucleation can occur at the solid–liquid interface.

A precipitate that has nucleated at the interface will grow into the melt with a growth velocity  $v_p$  (Fig. 8). It depends on the number of impurity atoms that can be transported to the precipitate by diffusion in the melt. Since the melt interface proceeds at the same time with a velocity  $v$ , the final

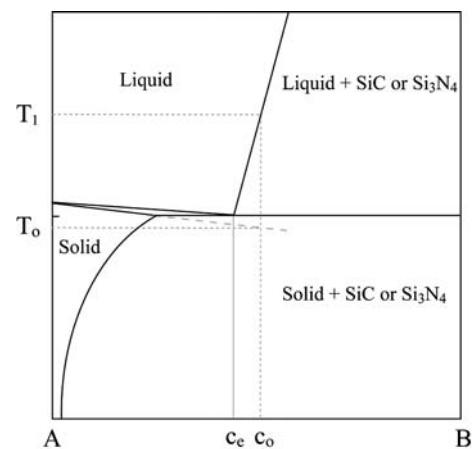


**Fig. 7** Schematic phase diagram for carbon and nitrogen. A: Si, B: C or N. For explanation see text

size of the precipitate is determined by the competition of the advancing solidification front and the precipitate growth. If  $v > v_p$ , the precipitate will be overgrown and incorporated into the solid. If  $v < v_p$ , the precipitate will grow into the melt and the process will be slowed down or stop because the impurity concentration decreases in front of the melt interface. If  $v = v_p$ , precipitate growth and interface proceed at the same velocity, and long precipitates can grow in the direction of crystallization.

This steady state situation has been analyzed numerically by solving the time-independent diffusion equation for different precipitate geometries, namely layers and rods. Numerical estimations show that very long precipitates of several millimeters can occur depending on the supersaturation,

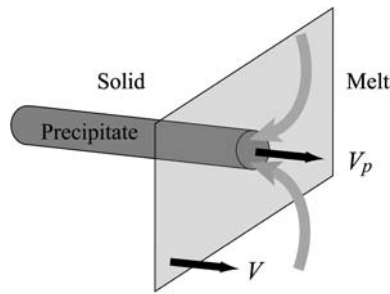


**Fig. 8** Schematic presentation of the growth of a rod-like precipitate at an advancing melt interface.  $V$ ,  $V_p$ : growth velocity of Si-solidification front and precipitate, resp.

the interface velocity and the temperature gradients at the melt interface. Whether rod-like or planar structures of the precipitate form depends on the crystallography and interface energies of the phases that form. Obviously, planar precipitates are preferred for SiC in twin boundaries and filament structures for  $\text{Si}_3\text{N}_4$ .

For very high supersaturations of carbon and nitrogen in the melt, precipitation may even occur in front of the melt interface. Large particles may also break out of the powdery  $\text{Si}_3\text{N}_4$  coating and be transported directly into the melt without complete dissolution. In both cases, the precipitates are finally incorporated by the advancing interface. It has also been suggested that larger particles are pushed by the advancing melt interface before incorporation [29]. This may explain why sometimes very large precipitates or inclusions (up to millimeters in size) of SiC and  $\text{Si}_3\text{N}_4$  are observed in the solid.

Other impurities, such as oxygen or metallic impurities, never reach such high concentrations in the silicon melt, so that this melt growth mechanism cannot operate. This is in agreement with the observation that the formation of large precipitates ( $\gg 10 \mu\text{m}$ ) does not occur here. By controlling the oxygen, carbon and nitrogen dissolution from the crucible, the incorporation over the gas atmosphere and the convection in the melt one can suppress the precipitate formation at the melt interface and reduce the amount of impurities that are incorporated in the solid.

## 4 Precipitate formation in the solid

### 4.1 Oxygen, carbon and nitrogen

The distributions of dissolved oxygen, carbon and nitrogen in the solid show features typical for the different growth processes, which correspond to their distribution pattern in the melt as discussed before. In the ingot techniques (Bridgman, VGF), oxygen with a segregation coefficient  $k_0 > 1$  shows a decrease in the concentration of the dissolved species along the growth direction from the bottom to

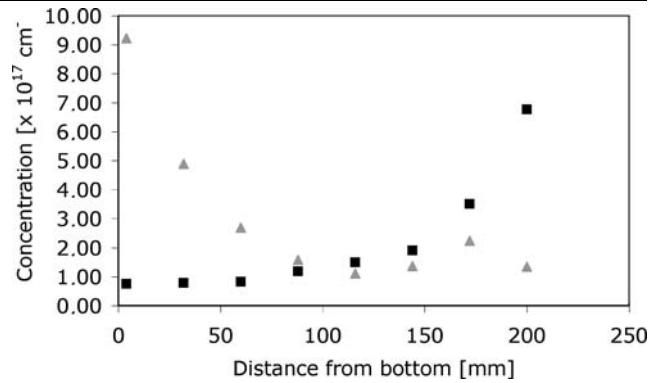


**Fig. 9** FTIR measurements of interstitial oxygen ( $\text{O}_i$ ) and substitutional carbon ( $\text{C}_s$ ) along the growth direction in the center of a mc-silicon crystal grown by the ingot technique

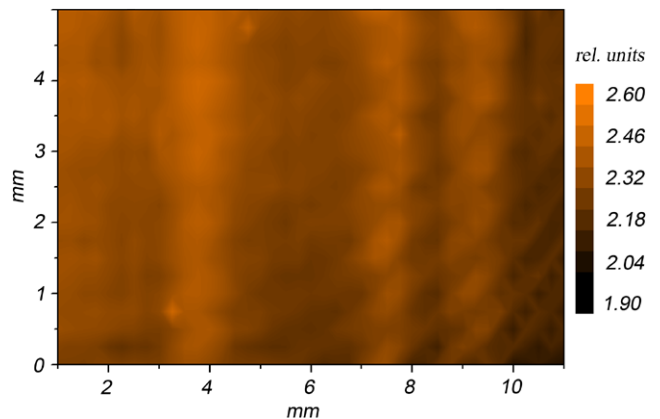


**Fig. 10** Topographic FTIR measurement of the distribution of dissolved carbon in an EFG wafer. The concentration is given in relative units. Absolute concentrations are obtained by multiplying with  $5 \times 10^{17} \text{ cm}^{-3}$ . The growth direction is vertical

the top of the solidified crystal. For carbon and nitrogen with  $k_0 < 1$ , the concentration increases. Figure 9 shows typical distributions of the dissolved species measured with Fourier Transformed Infrared (FTIR) spectroscopy.

In growth techniques, where the melt is continuously replenished with fresh, pure silicon the distribution of the elements remains stationary over long periods of time. This is the case for the EFG ribbon growth, where the main impurity is carbon. Figure 10 shows the dissolved carbon distribution in the solid ribbons. It is characterized by concentration variations of about 40% perpendicular to the growth direction. The origin has not been determined yet, but may lie in temperature variations across the side faces of the octagon tube. In general, the carbon concentrations are close to or above the maximum solubility limit at the melting point. The concentrations of oxygen and nitrogen in EFG silicon are much lower compared to ingot silicon ( $< 1 \times 10^{16} \text{ cm}^{-3}$  for oxygen,  $< 3 \times 10^{15} \text{ cm}^{-3}$  for nitrogen) and are less relevant [30].

The precipitation behavior of these elements in mono-crystalline silicon is well known and shall not be discussed

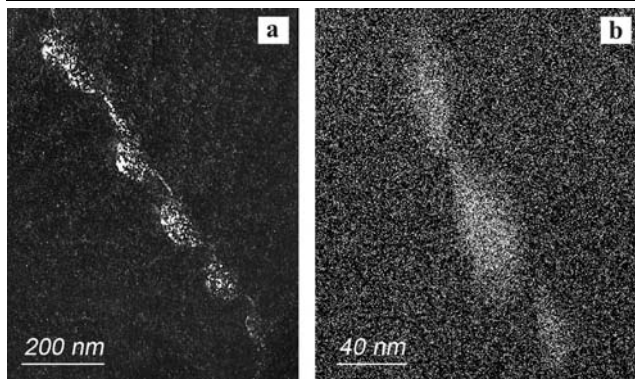


**Fig. 11** Transmission electron microscopy image of clusters of oxygen precipitates at a dislocation (a). Energy filtered TEM image showing the oxygen distribution in part of the same area (b)

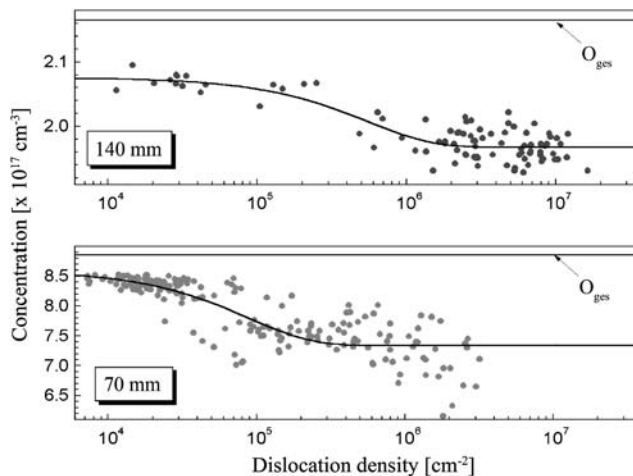


**Fig. 12** FTIR measurement of the oxygen concentration in dislocated areas as a function of the dislocation density and comparison with the total oxygen concentration in the same area. Measurements at two different positions in a mc-silicon crystal along the growth direction

here (for an overview see [31–33]). An important new aspect in multicrystalline silicon, which has a much higher defect density, is the interaction of impurities with dislocations and grain boundaries. Because of the disturbed crystal structure at the core of the extended defects, impurities can accumulate there. Therefore, in the as-grown material the total concentration of the elements consists of the dissolved species and the fraction accumulated at the extended defects during crystal growth.

Systematic results have been obtained for oxygen in ingot silicon. Transmission Electron Microscopy (TEM) in combination with chemical (EDX) analyses shows an enrichment of oxygen at dislocations (Fig. 11). The accumulation of oxygen in the strain field of the dislocation is accompanied by the nucleation of small  $\text{SiO}_2$  precipitates. The total oxygen concentration  $c_{\text{tot}}$  can be determined experimentally by annealing the crystal above the solubility temperature. The gettered oxygen is released then into the bulk, where

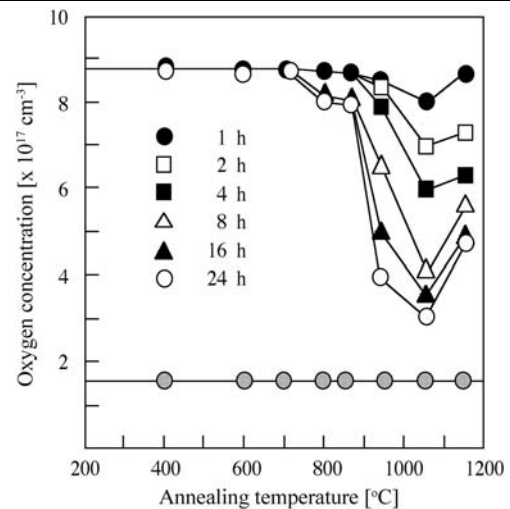


**Fig. 13** FTIR measurement of the change in interstitial oxygen concentration in mc-silicon after annealing for two different initial oxygen concentrations

it can be determined by FTIR as interstitial oxygen. Figure 12 shows that in regions of higher dislocation densities more oxygen has been gettered and that  $c_{\text{tot}}$  decreases with the ingot height in correspondence with the oxygen distribution along the growth direction. The results also show that a large fraction of these elements remains in supersaturation in the as-grown crystals probably because of the limited time available for precipitation during the cooling phase of the crystals.

First, subsequent annealing for longer periods of time leads to massive precipitation. FTIR investigations of the interstitially dissolved oxygen in ingot silicon show that the concentration decreases considerably in the temperature regime between 700–1100 °C depending on the annealing time (Fig. 13). Part of the oxygen accumulates at dislocations then. In addition, bulk precipitates are observed if the starting concentrations are above  $3 \times 10^{17} \text{ cm}^{-3}$ . Two types are observed: platelike crystalline precipitates, which form at temperatures below 800 °C, and spherical amorphous  $\text{SiO}_2$  precipitates at higher temperatures (Fig. 14). Due to the decreasing oxygen concentration to the top of the ingot bulk, precipitation ceases and is not observed anymore.

Precipitation of carbon is, in general, a very slow process because of the low diffusion coefficient in the solid [34]. At carbon concentrations between  $6 \times 10^{16}$ – $6 \times 10^{17} \text{ cm}^{-3}$  in ingot silicon the solubility limit is reached between about 1200–1400 °C. At these temperatures, the diffusivity is already so slow that most of the carbon remains dissolved after crystal growth. If  $\text{SiC}$  precipitates occur, they are either small ( $< 1 \mu\text{m}$ ) or, if larger, have been nucleated in the melt by the mechanisms described in Sect. 3. In EFG ribbons, where the carbon concentration is close to or even above the maximum solubility,  $\text{SiC}$  should precipitate directly after solidification. Due to the fast cooling rate after solidifi-

**Fig. 14** TEM images of platelike crystalline (a) and spherical amorphous (b) oxygen precipitates in mc-silicon

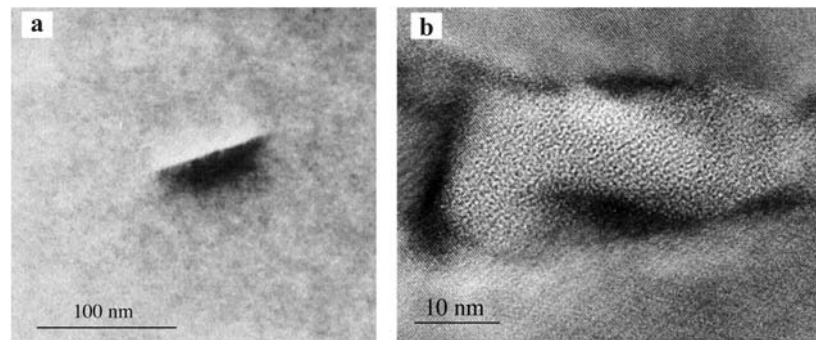
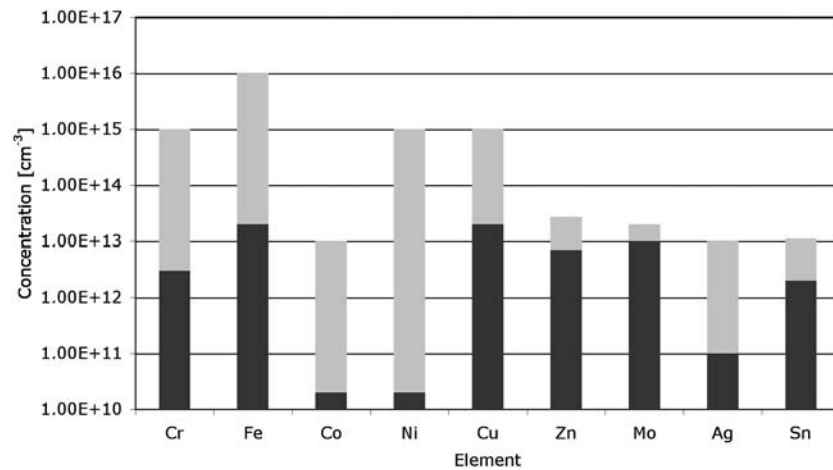


**Fig. 15** Neutron activation analyses of the concentrations of metallic impurities in feedstock silicon. Light bars indicate the concentration range for different materials



cation, precipitation is also suppressed, however. Recently, it has been proposed for EFG ribbons that nanometer size SiC precipitates still form in the bulk, which may be recombination active [30]. A direct observation, however, was not possible yet, probably because of the very low density.

#### 4.2 Metal impurities

Much less is known about the distribution of metal impurities in multicrystalline silicon. Measurements of the total concentration by the Neutron Activation Analyses (NAA) method show large variations for different materials (Fig. 15). This is partly due to impurity variations in the feedstock silicon for the crystal growth. In general, the concentrations are orders of magnitude higher compared to the concentrations of the dissolved species that are determined by electrical measurement techniques. Therefore, one must assume that the largest fraction of the impurities are trapped in an electrically inactive or less active form, most likely at extended defects, such as dislocations, grain boundaries and precipitates of other elements like oxygen, carbon and nitrogen.

The most relevant metal impurities have very low segregation coefficients  $k_0 \ll 1$ . Therefore, one can expect that in ingot growth the concentrations increase in growth direction from the bottom to the top of the solidified crystal. The

concentration  $c_s$  in the solid can often be described by the Scheil equation, which is valid for complete mixing of the melt and  $x < 0.9$

$$c_s = k_{\text{eff}} c_0 (1 - x)^{k_{\text{eff}} - 1}, \quad (1)$$

where  $x$  is the fraction of solidified solid,  $k_{\text{eff}}$  an effective segregation coefficient and  $c_0$  the melt concentration. Particularly for the metals with a high diffusivity, deviations of this pattern may occur near the edges of the ingots due to the in-diffusion of further foreign atoms from the contact with crucible walls during the cooling phase. The contaminated regions extend here about 1–2 cm and cannot be used for solar cells with a high efficiency. Since the impurities are also enriched in the top region, where the melt solidifies last, they may diffuse backwards into the bulk if the region stays at elevated temperatures for some time. This back-diffusion has been observed for some metals, such as Fe, Co and Cu [35], and can lead to a modified concentration profile (Fig. 16).

In general, precipitation of metal impurities during cooling is rarely observed in multicrystalline silicon. Considering that most of the metals are accumulated at dislocations and grain boundaries and very high concentrations may be reached, one might expect precipitation there. X-ray fluorescence investigations of less pure mc-silicon using synchrotron radiation have shown that nano-scale iron silicate



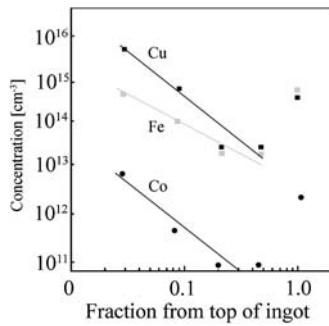


**Fig. 16** Measurement of the distribution of some metal impurities in mc-silicon. (The growth direction is from *bottom* to *top*)

precipitates may occur at grain boundaries [36, 37]. However, very small (nanometer size) precipitates are difficult to detect because of their small size and low density. The experimental results so far indicate that most of the metallic impurities are accumulated at extended defects without precipitation.

## 5 Dislocation formation during crystal growth

The microstructures of multicrystalline silicon materials differ considerably depending on whether the material is grown by an ingot or a sheet growth technique. In ingot silicon, the average dislocation densities vary between  $10^4$  and  $10^6$   $\text{cm}^{-2}$ , but locally bundles of dislocations with densities higher than  $10^8$   $\text{cm}^{-2}$  occur and can extend over several centimeters in growth direction (Fig. 17). In EFG ribbons, the microstructure is dominated by heavily twinned regions where hundreds of (111) twin boundaries extend in growth directions over several centimeters. The width of the twin lamella is in the micrometer range. In the twinned regions, the dislocation density is below  $10^3$   $\text{cm}^{-2}$ , whereas outside it varies between  $10^4$  and  $10^6$   $\text{cm}^{-2}$  with high local densities (Fig. 6(a)).

Dislocations are formed during crystal growth by plastic deformation to reduce the thermal stresses. In EFG ribbons, the stress relief occurs partly by twinning; therefore, these regions remain mainly dislocation free. The main feature of the dislocated areas is the inhomogeneous distribution of dislocations with high local densities. Some of these dislocation networks show high recombination rates and are thus very detrimental to the lifetime of minority charge carriers [38, 39]. In addition, these dislocations are partly difficult to passivate and thus remain active even in the solar cell.

The origin of the local high densities is not understood, yet. It could be shown that dislocation bundles extend over several centimeters in growth direction once they have formed. Since it is difficult to locate the nucleation point of a bundle in a large crystal, not much is known about the stress

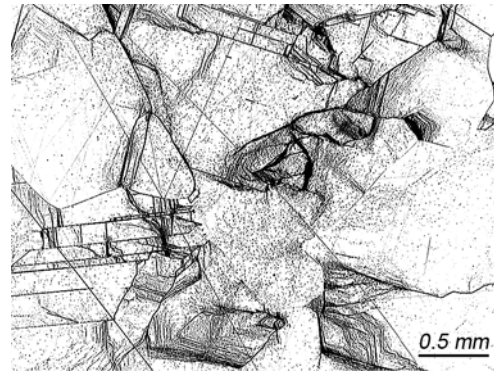


**Fig. 17** Etch pit measurement of the dislocation distribution in a mc-silicon wafer grown by the ingot technique

concentrations that have caused the high local density. Possible mechanisms are the anisotropic thermal expansion of neighboring grains or strong lattice distortions around certain types of precipitates (e.g., silicon dioxide).

The average dislocation density can however be predicted sufficiently well with the Alexander–Haasen model [40, 41]. This model has been developed to describe the early stages of the plastic deformation of semiconductor single crystals. It is based on a physical description of the motion and multiplication of dislocations in the crystal. The basis is the multiplication law for the density  $N$  of the mobile dislocations, which is equal to the total density for the early stages of deformation

$$\frac{dN}{dt} = kNv_d\tau_{\text{eff}}, \quad (2)$$

where  $k$  is a proportionality constant,  $v_d$  is the dislocation velocity and  $\tau_{\text{eff}}$  the effective stress driving the dislocations. The dislocation velocity depends on the temperature and the stress

$$v_d = v_{d0}\tau_{\text{eff}}^m e^{-U(\tau_{\text{eff}})/k_B T}, \quad (3)$$

where  $U(\tau_{\text{eff}})$  is the activation energy of dislocation mobility,  $m$  a stress exponent, which is close to one, and  $k_B$  the Boltzmann constant. For stresses below about 20 MPa, the activation energy of the  $60^\circ$  dislocation increases up to 2.5 eV. The effective stress  $\tau_{\text{eff}}$  is a sum of different contributions

$$\tau_{\text{eff}} = \tau - A\sqrt{N} - G\varepsilon_{\text{pl}} \quad (4)$$

with

$$A = Gb/2\pi(1 - \nu),$$

where  $\tau$  is the external stress acting on the dislocation. In crystal growth, it is produced by thermal stresses  $\tau_{\text{th}}$  in the crystal. The second term considers the repulsive interaction with other (mobile and sessile) dislocations, which hinder

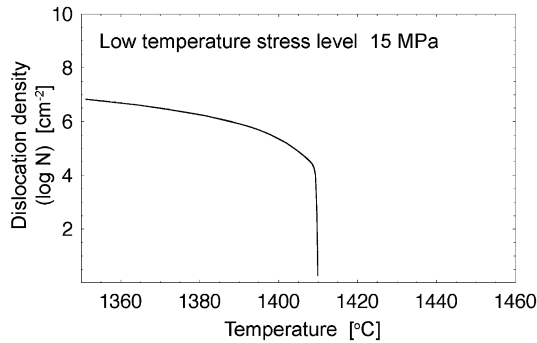


**Fig. 18** Calculated dislocation density as a function of the decreasing temperature during cooling of a solidified silicon crystal. The following values have been used for the calculation:  $k = 0.031$  cm/N,  $v_0 = 4.3 \times 10^6$  cm/s,  $m = 1.1$ ,  $U = 2.18$  eV,  $b = 0.384$  nm,  $G = 61.5$  GPa. For definition of terms see text

the motion.  $G$  is the shear modulus,  $b$  the Burgers vector, and  $\nu$  is the Poisson's number. In numerical simulations,  $A$  may also be treated as a free parameter. The third term comes from the stress relaxation through plastic deformation. It is described by the Orowan relation

$$\frac{d\varepsilon_{pl}}{dt} = bNv_d. \quad (5)$$

The various parameters have been determined experimentally from single crystal deformation experiments for silicon [41]. A numerical solution of the (2–5) for a constant thermal stress and an exponential time dependence of the temperature ( $T_m$  melting temperature)

$$T = T_m e^{-t/t_0} \quad (6)$$

is shown in Fig. 18 for silicon. An initial density of nucleation sites  $N_0$  is assumed here, but the final results are almost independent on the starting value for  $N_0 < 100$ . The results show that there is a steep increase of the dislocation density within the first degrees below the melting point followed by a gradual increase depending on the stress level. Below about 1000°C the dislocation density remains almost constant. Depending on the stress level, the final dislocation density can vary between  $10^4$  and  $10^8$  cm $^{-2}$ . This is in the regime that is observed experimentally. During the sharp initial increase in the density the dislocations move over large distances of several centimeters (Fig. 19). Considering that the grain sizes in a mc-crystal are less than one centimeter, these dislocations will be blocked by grain boundaries. This may be another reason for the observed inhomogeneous distribution of the dislocation density.

There are still uncertainties in the results because some of the used parameters are not known exactly. An important parameter is the activation energy  $U$  of the dislocation velocity. Experimental results are only available in the temperature regime up to 1250°C. It is assumed so far that it

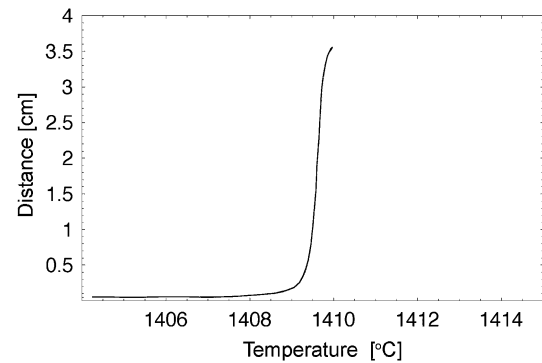


**Fig. 19** Calculated distance of the path length of nucleated dislocations as a function of the decreasing temperature during cooling of a solidified silicon crystal

has the same value and stress dependence up to the melting temperature.

Realistic simulations have to determine the thermal stresses during a crystal growth. The temperature distribution in a furnace and during crystal growth can be calculated today with sufficient accuracy by FEM simulations [42]. Therefore, thermal stresses can be calculated from local temperature differences  $\Delta T$  according to

$$\tau_{th} = K\alpha\Delta T, \quad (7)$$

where  $\alpha$  is the thermal expansion coefficient and  $K$  the compression modulus of the solid. In some cases, such calculations have been combined with the Alexander–Haasen model to determine the evolution of the dislocation density [42, 43]. FEM simulations of large crystals determine the temperature on a length scale of about one centimeter. The crystals are treated as an isotropic solid, and the stress components are averaged over a large volume using the von Mises criterion [44–46]. Therefore, the simulations at present do not allow simulating the local variations that are observed on the micrometer scale. Improvements are possible by taking into account the local polycrystalline structure. Then stress components on each (111) glide plane can be determined and the orientation dependence of the dislocation motion taken into account. Local calculations on a finer scale require a multi-scaling approach which is much more sophisticated. Such calculations have not been tried, yet. They would allow one to determine the influence of parameters such as crystal orientation, change in the dislocation velocity due the interaction with foreign atoms, or variations in the temperature cooling profile during crystal growth. Nonetheless, the present level of simulations gives agreement with experimental results within an order of magnitude and allows optimizing the growth process already to some extent.

## 6 Recombination behavior of extended defects

Dislocations, grain boundaries and precipitates are recombination centers for minority charge carriers. In multicrystalline silicon, grain boundaries are less important because of their low density. Bulk precipitation only occurs for oxygen, carbon and nitrogen under special growth conditions as described before. Metal precipitation so far has only been observed at dislocations or grain boundaries. Therefore, their impact on the recombination will be discussed in connection with the dislocation behavior.

### 6.1 Recombination at precipitates

Precipitates of carbon, nitrogen and oxygen are detrimental for solar cells in several ways. Large precipitates ( $> 10 \mu\text{m}$ ), in particular of SiC, are hard particles, which aggravate wafer cutting or the fabrication of electrical contacts. SiC precipitates can also be electrically conductive and provide shunting paths through the pn-junction of a solar cell, which reduces the performance and efficiency. Smaller sub-micrometer precipitates that nucleate in the solid during the cooling phase of crystal growth can also reduce the lifetime.

This is particularly known for oxygen precipitates in monocrystalline silicon, which have been thoroughly studied over decades [31–34]. The electrically active defects connected with the precipitates are known as New Donors. They are bandlike, deep donor states, which are believed to be related to interface defects between oxide precipitate and silicon lattice. They form in the temperature range between 700 and 1000°C. Investigations on multicrystalline silicon show that similar defects also occur here [47]. Figure 20 depicts the dependence of the lifetime on the amount of precipitated oxygen, which has been determined from FTIR measurements. TEM investigations showed that the previously described platelike SiO<sub>2</sub> precipitates (Fig. 14) are responsible for the electrical activity. These defects form after annealing below about 800°C. Whether or not they grow already in the as-grown crystals depends on the initial oxygen concentration and the dwelling time during cooling in the critical temperature regime.

The influence of small, submicrometer, carbon and nitrogen precipitates on the lifetime is less clear because such precipitates have not been observed so far. EFG ribbons have carbon concentrations (up to  $9 \times 10^{17} \text{ cm}^{-3}$ ) higher than the solubility limit and show a reduced lifetime in regions of low dislocation density. Possibly, the underlying recombination activity results from nanosized SiC precipitates that can be assumed, as recently suggested, to have formed due to the high C content [30]. Carbon and nitrogen can enhance the nucleation of oxygen precipitates; therefore, an alternative explanation could be that the observed recombination centers are induced small oxygen precipitates. Since the oxygen

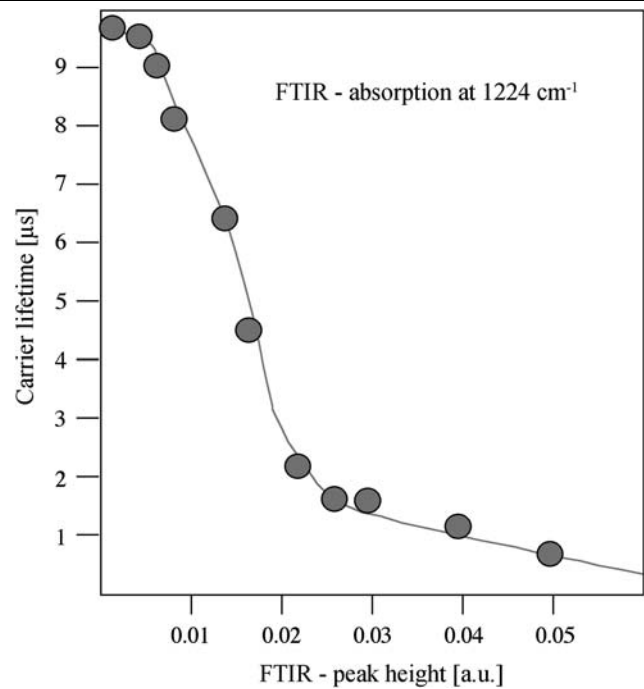


**Fig. 20** Minority carrier lifetime in a p-doped mc-silicon crystal as a function of precipitated oxygen. The fraction of precipitated oxygen is determined from the peak height of FTIR absorption spectra corresponding to SiO<sub>2</sub> precipitates

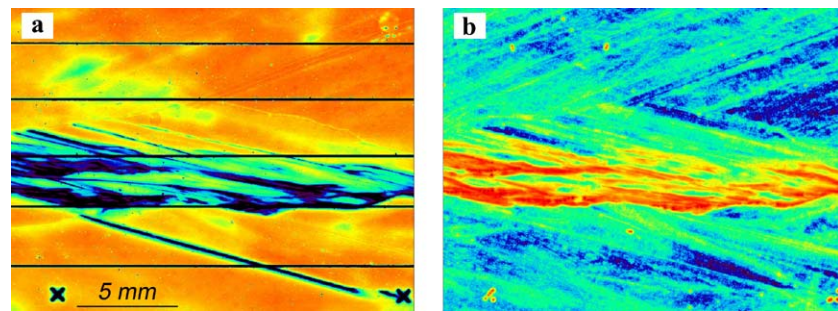
and nitrogen concentrations are below the detection limit ( $< 3 \times 10^{15} \text{ cm}^{-3}$  for interstitial O<sub>i</sub> and  $< 2 \times 10^{14} \text{ cm}^{-3}$  for N<sub>2</sub>), the formation of carbon induced oxygen precipitates, which can be observed for higher oxygen concentrations, is however unlikely here.

### 6.2 Recombination at dislocations

Dislocations can be efficient recombination centers for minority charge carriers. Since they partly occur in dense networks these regions are very detrimental to the lifetime. In addition, dislocation bundles are often difficult to passivate in the solar cell process and thus reduce the efficiency. Experimental investigations of the recombination activity of individual dislocations have shown that it depends on the contamination with impurities and can change considerably [48]. Typical experimental methods, such as Electron Beam Induced Current (EBIC) or Photoluminescence spectroscopy (PL), are difficult to apply quantitatively if one wants to investigate the average behavior of many dislocations in networks. Here, other methods are more suitable.

A recently developed method for solar cells is depicted in Fig. 21. A larger area is measured topographically by the Light Beam Induced Current (LBIC) technique. The solar cell is illuminated locally and the light induced current measured. Simultaneously, the reflected light can be measured, which allows one to convert the LBIC signal into the local internal quantum efficiency (IQE). In the same area, the

**Fig. 21** Internal quantum efficiency (IQE) map measured by the light beam induced current (LBIC) technique (a) and corresponding dislocation density map (b) in a multicrystalline silicon solar cell



dislocation density is determined by etch pit counting after removing the contact structure of the cell. The IQE values and the dislocation density are correlated then locally. If the recombination properties of the dislocations in the investigated region are equal, one obtains diagrams as shown in Fig. 22. A typical feature is the reduction of the IQE at higher dislocation densities, i.e., above about  $10^5 \text{ cm}^{-2}$ .

The IQE values can be converted into the local diffusion length  $L_D$  of minority charge carriers using solar cell simulation programs. In the present case, the one-dimensional PC1D program is used. The diffusion length data can be fitted very well to a theoretical model developed by Donolato [49]. In combination with the commercial PC1D program, one can also fit IQE values directly to the dislocation density data [50–53]. One obtains two parameters: the bulk diffusion length  $L_0$  (without dislocations) and the normalized recombination strength of the dislocations  $\Gamma = V_D/D$ .  $V_D$  is the dislocation recombination velocity and  $D$  the diffusion coefficient of the minority carriers. Whereas the bulk diffusion length is constant over large areas of a solar cell,  $\Gamma$  varies typically between  $\Gamma = 0.0001$ – $0.001$ . These variations can be explained by different degrees of contamination with mainly metallic impurities.

The same technique can also be applied to wafers before solar cell processing. Here the diffusion length can be measured directly with the Surface Photovoltage (SPV) method. Some results are shown in Fig. 23 for EFG ribbon material. The correlation of the data and fitting them to the Donolato model yields  $\Gamma = 0.003$ . This comparatively high value indicates that the dislocations have a higher degree of contamination. Since the performance of the EFG solar cells is similar to that of ingot silicon, the gettering and passivation processes can still efficiently reduce the recombination of the dislocations.

## 7 Summary

The presented results show that extended defects in multicrystalline silicon come into existence in different temperature regimes during crystal growth. Large precipitates of oxygen, carbon and nitrogen can nucleate first at the melt

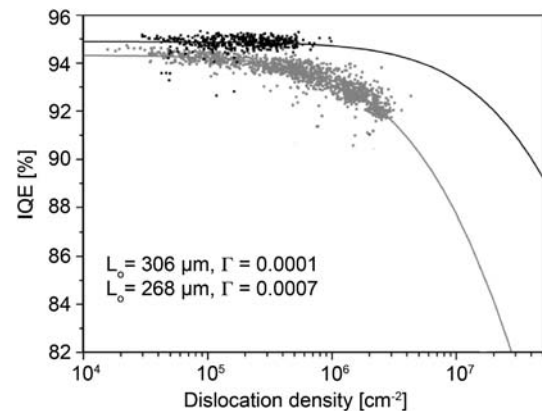


**Fig. 22** Local correlation of IQE values with the dislocation density in a multicrystalline silicon solar cell. Fitted curves from the Donolato–Rinío (see text) model yield bulk lifetime  $L_0$  and average recombination strength  $\Gamma$  of the dislocations

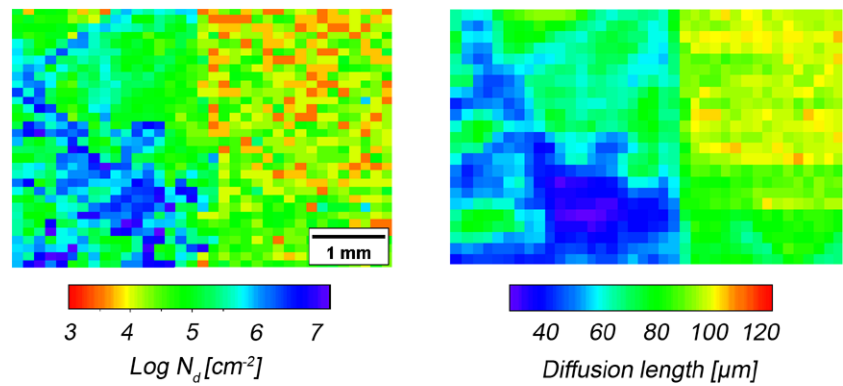
interface. This process depends on the impurity level in the melt and at the solidification front. It can be suppressed by controlling the interaction with the crucible, the gas flow over the melt and the convection in the melt.

Dislocations form immediately after solidification and their density increases during cooling down to temperatures of about  $1000^\circ\text{C}$ . Keeping the thermal stresses low during cooling, one can reduce the dislocations density to levels below  $10^5 \text{ cm}^{-2}$ . It is not clear yet how to avoid the observed local regions of high density. In combination with improved numerical simulations of the dislocation density one may be able to identify temperature regimes which are particular harmful. A further possibility to reduce the dislocation density is to modify the dislocation velocity by solid solution hardening. A possible candidate is germanium that is an isoelectronic element in silicon and causes a strong lattice distortion.

When the solubility limit of impurities is exceeded precipitation may occur. Carbon and oxygen are the impurities with the highest concentrations. Carbon precipitation is so slow that it may only occur at very high impurity concentrations such as in EFG ribbon silicon. Whether SiC precipitates of nanometer size occur could not be confirmed, yet. Indirect evidence is derived from lifetime measurements



**Fig. 23** Diffusion length map measured by the surface-photovoltage-technique (right) and corresponding map of the dislocation density  $N_d$  (left) in a multicrystalline silicon wafer



in EFG ribbons. Oxygen at the concentrations levels observed for mc-ingot silicon begins to precipitate below about 1100°C. Since the precipitates are rather detrimental, this process has to be avoided either by reducing the oxygen level or by reducing the time for growth.

Metallic impurities occur in very high concentrations so far. They are mostly trapped at the dislocations and grain boundaries but are released into the bulk during solar cell processing. The gettering takes place at temperatures below 600°C depending on the impurity. The contamination of the dislocations (and grain boundaries) increases their recombination activity. On the other hand, the metal impurities are removed from the bulk, where they are even more detrimental.

Many details of the interaction mechanisms between impurities and dislocations are still not known enough. At present a reduction of the contamination appears difficult to achieve considering that most of the impurities have to be gettered at these defects to keep the bulk impurity concentration at acceptable levels. One would need a substantial reduction by several orders of magnitude in the total metal concentration to see an impact on the degree of contamination. The control of the extended defects to improve the performance of the silicon requires still a much better understanding of the defect behavior during crystal growth and the subsequent solar cell processing.

## References

1. A.D. Little, in *Proc. 16th Europ. Photovolt. Solar Energy Conf.*, ed. by H. Scheer, B. McNelis, W. Palz, H.A. Ossenbrink, P. Helm (James & James, London, 2000), p. 9
2. A. Endrös, D. Franke, Ch. Häbeler, J. Kaleis, W. Koch, H.J. Möller, *Handbook of Photovoltaic Engineering* (Wiley-VCH, Weinheim, 2002), p. 634
3. H. Lautenschlager, F. Lutz, C. Schetter, U. Schubert, R. Schindler, in *Proc. 14th Europ. Photovolt. Solar Energy Conference* (Stephens & Associates, Bedford, 1997), p. 1358
4. J.M. Gee, R.R. King, K.W. Mitchell, in *Proc. IEEE 25th Photovolt. Specialist Conference*, ed. by P. Basore (IEEE, New York, 1996), p. 409
5. O. Schultz, S.W. Glunz, G. Willeke, A. Leimenstoll, H. Lautenschlager, J.C. Goldschmidt, in *Proc. 19th Europ. Photovolt. Solar Energy Conference* (Stephens & Associates, Bedford, 2004), p. 817
6. A. Müller, M. Ghosh, R. Sonnenschein, P. Woditsch, *Mater. Sci. Eng. B* **134**, 257 (2006)
7. H.A. Aulich, F.-W. Schulze, J. Grabmeier, *Chemie Ingenieur Technik* **56**, 667 (1984)
8. H. de Moor, A. Jäger-Waldau, in *Proc. PVNET Workshop Proceedings "RTD Strategy for PV"*, Special Publication: S.P.I. 02.117 (European Commission, DG Joint Res. Centre, Ispra, 2002)
9. J. Dietl, D. Helmreich, E. Sirtl, *Crystals*, vol. 5 (Springer, Berlin, 1981), p. 43
10. M. Rinio, S. Peters, M. Werner, A. Lawrenz, H.J. Möller, *Solid State Phenom.* **82–87**, 701 (2002)
11. H.J. Möller, in *Handbook of Semiconductor Technology—Electronic Structure and Properties of Semiconductors*, ed. by K.A. Jackson, W. Schröter, vol. 1 (Wiley-VCH, Weinheim, 2000), p. 715
12. R. Kawamura, K. Sasatani, T. Onizuka, *Sol. Energy Mater. Sol. Cells* **49**, 307 (1997)
13. H. Lange, I. Schwirtlich, *J. Cryst. Growth* **104**, 108 (1990)
14. A. Goetzberger, A. Räuber, in *Techn. Digest of 9th Int. Photovolt. Solar Energy Conference*, ed. by W. Palz, G.T. Wrixon, P. Helm (Kluwer Academic, Dordrecht, 1989), p. 4
15. J.I. Hanoka, *Sol. Energy Mater. Sol. Cells* **65**, 231 (2001)
16. M. Bellmann, Dissertation, TU Bergakademie Freiberg, 2007
17. A.K. Søiland, E.J. Øvrelid, T.A. Engh, O. Lohne, J.K. Tuset, Ø. Gjerstad, *Mater. Sci. Semicond. Process.* **7**, 39 (2004)
18. A. Lawrenz, M. Ghosh, K. Kremmer, V. Klemm, A. Müller, H.J. Möller, *Solid State Phenom.* **95/96**, 501 (2004)
19. C. Reimann, J. Friedrich, G. Müller, S. Würzner, H.J. Möller, in *Proc. 22th European Photovoltaic Solar Energy Conference* (WIP/ETA, München/Mailand, 2007), p. 1073
20. U. Gösele, T.Y. Tan, *Appl. Phys. A* **28**, 79 (1982)
21. H. Föll, U. Gösele, B.O. Kolbesen, *J. Cryst. Growth* **52**, 907 (1981)
22. P.M. Petroff, A.J.R. de Kock, *J. Cryst. Growth* **30**, 117 (1975)
23. S. Möller, H.J. Möller, in *Proc. 9th PV Solar Energy Conf.* (Kluwer Academic, Dordrecht, 1989), p. 439
24. S. Rajendran, M. Larrousse, B.R. Bathey, J.P. Kalejs, *J. Cryst. Growth* **128**, 338 (1993)
25. H.J. Möller, *Solid State Phenom.* **95/96**, 181 (2004)
26. M. Werner, K. Scheerschmidt, E. Pippel, C. Funke H, J. Möller, in *Proc. 12th Int. Conf. on Microscopy of Semiconducting Material*, Inst. Phys. Conf. Ser. No. 34 (2003), p. 232
27. J.P. Kalejs, B. Chalmers, *J. Cryst. Growth* **79**, 487 (1986)
28. H.J. Möller, *MRS Symp. Proc.* **205**, 476 (1991)
29. K.A. Jackson, J.D. Hunt, *Trans. Metall. Soc. AIME* **236**, 1129 (1966)

30. S. Scholz, Dissertation, TU Bergakademie Freiberg, 2008
31. J.C. Mikkelsen, S.J. Bearton, J.W. Corbett, S.J. Pennycook (eds.), *Oxygen, Carbon, Hydrogen and Nitrogen in Crystalline Silicon*. Mat. Res. Soc. Symp. Proc., vol. 59 (Mater. Res. Soc., Warrendale, 1986)
32. W. Bergholz, *Semiconductors and Semimetals*, vol. 42 (Academic Press, New York, 1994), p. 513
33. in *Defects in Silicon II* (The Electrochemical Soc., Pennington, 1991)
34. R. Newman, J. Wakefield, J. Phys. Chem. Solids **19**, 230 (1961)
35. D. Macdonald, A. Cuevas, A. Kinomura, Y. Nakano, L. Geerligs, J. Appl. Phys. **97**, 033523 (2005)
36. A.A. Istratov, W. Huber, E.R. Weber, Appl. Phys. Lett. **85**, 4472 (2004)
37. S. McHugo, A. Thompson, A. Mohammed, G. Lamble, I. Perichaud, S. Martinuzzi, M. Werner, M. Rinio, W. Koch, H. Höfs, C. Hässler, J. Appl. Phys. **89/8**, 4282 (2001)
38. S. Pizzini, A. Sandrinelli, M. Beghi, D. Narducci, F. Allegretti, S. Torchio, G. Fabbri, P. Ottaviani, F. Demartin, A. Fisi, J. Electrochem. Soc. **135**, 155 (1988)
39. B. Sopori, L. Jastrzebski, T. Tan, S. Narayanan, in *12th European Photovoltaic Solar Energy Conference* (ETA, Amsterdam, 1994), p. 1003
40. H. Alexander, P. Haasen, Solid State Phys. **22**, 27 (1968)
41. H. Alexander, *Dislocations in Solids* (Elsevier, London, 1986), p. 114
42. D. Franke, Dissertation, RWTH, Aachen, 2000
43. N. Banos, J. Friedrich, G. Müller, J. Cryst. Growth (2008, in press)
44. C.T. Tsai, M.W. Yao, A. Chait, J. Cryst. Growth **125**, 69 (1992)
45. C.T. Tsai, O.W. Dillon, R.J. de Angelis, J. Eng. Mater. Technol. **112**, 183 (1990)
46. X.A. Zhu, C.T. Tsai, J. Appl. Phys. **97**, 43520 (2005)
47. D. Yang, H.J. Möller, Solid State Phenom. **82–84**, 707 (2002)
48. S. Scholz, F. Dreckschmidt, T. Kaden, H.J. Möller, A. Seidl, in *Proc. 21th European Photovoltaic Solar Energy Conference* (WIP/ETA, München/Dresden, 2006), p. 354
49. C. Donolato, J. Appl. Phys. **84**, 2656 (1998)
50. M. Rinio, S. Peters, M. Werner, A. Lawerenz, H.J. Möller, Solid State Phenom. **82–84**, 701 (2002)
51. M. Rinio, A. Hauser, H.J. Möller, in *Proc. 3rd World Conf. on Photovolt. Energy Conversion*, ed. by K. Kurokawa, L. Kazmerski, B. McNelis, M. Yamaguchi, C. Wronski, W.C. Sinke (IEEE, New York, 2003), p. 847
52. A. Lawerenz, M. Rinio, S. Riedel, M. Ghosh, M. Werner, H.J. Möller, in *Proc. 16th Europ. Photovolt. Solar Energy Conf.* (James & James, London, 2000), p. 1647
53. P. Basore, D.A. Clugston, in *Proc. 25th IEEE Photovolt. Specialist Conf.* (IEEE, New York, 1996), p. 377